Passive scalars: Mixing, diffusion, and intermittency in helical and nonhelical rotating turbulence

P. Rodriguez Imazio[1,2] and P. D. Mininni[1]

[1]*Departamento de Física, Facultad de Ciencias Exactas y Naturales, Universidad de Buenos Aires and IFIBA, CONICET, Ciudad Universitaria, Buenos Aires 1428, Argentina*

[2]*Laboratoire de Physique Statistique, Ecole Normale Supérieure, CNRS, 24 rue Lhomond, 75005 Paris, France*

(Received 4 March 2015; revised manuscript received 3 December 2016; published 6 March 2017)

We use direct numerical simulations to compute structure functions, scaling exponents, probability density functions, and effective transport coefficients of passive scalars in turbulent rotating helical and nonhelical flows. We show that helicity affects the inertial range scaling of the velocity and of the passive scalar when rotation is present, with a spectral law consistent with $\sim k_\perp^{-1.4}$ for the passive scalar variance spectrum. This scaling law is consistent with a phenomenological argument [P. Rodriguez Imazio and P. D. Mininni, Phys. Rev. E **83**, 066309 (2011)] for rotating nonhelical flows, which follows directly from Kolmogorov-Obukhov scaling and states that if energy follows a $E(k) \sim k^{-n}$ law, then the passive scalar variance follows a law $V(k) \sim k^{-n_\theta}$ with $n_\theta = (5-n)/2$. With the second-order scaling exponent obtained from this law, and using the Kraichnan model, we obtain anomalous scaling exponents for the passive scalar that are in good agreement with the numerical results. Multifractal intermittency models are also considered. Intermittency of the passive scalar is stronger than in the nonhelical rotating case, a result that is also confirmed by stronger non-Gaussian tails in the probability density functions of field increments. Finally, Fick's law is used to compute the effective diffusion coefficients in the directions parallel and perpendicular to rotation. Calculations indicate that horizontal diffusion decreases in the presence of helicity in rotating flows, while vertical diffusion increases. A simple mean field argument explains this behavior in terms of the amplitude of velocity fluctuations.

DOI: 10.1103/PhysRevE.95.033103

I. INTRODUCTION

The study of passive scalar advection, mixing, and diffusion by anisotropic turbulence has gained more and more relevance over the years. Nowadays, it is well known that passive scalars share similarities with three-dimensional Navier-Stokes turbulence [1,2], presenting a direct cascade, anomalous scaling and intermittency [3,4]. Moreover, the study of passive scalar mixing in turbulent anisotropic flows is of interest in a wide variety of geophysical and astrophysical problems, such as the transport of chemical elements in rotating stars [5–7], the geodynamo [8], vertical transport and diffusion in the oceans [9,10], and the transport of pollutants and aerosols in the atmosphere [11].

Turbulent transport of passive scalars in rotating flows was previously studied in [12–14], although it has received less attention than the transport of passive scalars in isotropic turbulence [2,4,15]. Moreover, the effect of helicity in the passive scalar transport in rotating flows has been practically ignored so far. It is known that helicity plays a key role in many problems such as in the dynamo effect [16,17], and the effect of flow helicity in the transport of passive vectors has been the subject of study in astrophysics for many years [18]. Results in [19,20] for isotropic turbulence indicate that passive scalar transport is sensitive to whether the flow is helical or not. In laminar flows, and in particular in biological flows, it has been found that helicity enhances transport and mixing [21].

As helicity affects the direct cascade of energy in rotating flows [22], leading to a steeper energy spectrum, it is to be expected that the passive scalar cascade to smaller scales should also be affected by the presence of helicity (see, e.g., [14]). From this point, two questions naturally arise, which this work tries to answer: Is intermittency and the anomalous scaling of the passive scalar changed by the presence of helicity? And, how is the transport and mixing of the passive scalar affected? While the former question can be answered by computing scaling exponents for rotating flows with and without helicity, the latter requires quantification of the turbulent transport in directions parallel and perpendicular to the rotation axis.

The aim of this paper is then to characterize the turbulent scaling, transport, and diffusion of passive scalars in rotating helical flows. To this end, we use data from direct numerical simulations of the Navier-Stokes equations in a rotating frame plus the advection-diffusion equation for a passive scalar. We use a spatial resolution of 512^3 grid points in a regular periodic grid.

The analysis is divided in two parts. First, to study the effect of helicity in the turbulent scaling laws of the passive scalar, we calculate velocity and passive scalar spectra. We compute structure functions for the velocity and the scalar using an axisymmetric decomposition, and consider the corresponding scaling exponents to quantify intermittency in each field. We also calculate probability density functions (PDFs) for velocity field and passive scalar increments. As for nonhelical rotating turbulence (see [14]), we find that the passive scalar is more anisotropic than the velocity field at small scales. However, unlike the nonhelical rotating case, the passive scalar variance follows a spectral law consistent with $\sim k_\perp^{-1.4}$, where $k_\perp$ denotes wave vectors perpendicular to the rotation axis. This scaling is shallower than the one found in the nonhelical rotating case [14], and is correctly predicted by a simple phenomenological relation for the energy and passive scalar variance spectral indices. The passive scalar in the presence of helicity also becomes more intermittent than in the nonhelical rotating case.

Second, to study passive scalar diffusion, we compute effective anisotropic transport coefficients using the method used

first in [23] for stratified flows, and later in [14] for rotating nonhelical flows. Effective transport coefficients are obtained by studying the diffusion of an initial concentration of the passive scalar, and calculated using Fick's law by measuring the average concentration and average spatial flux of the scalar as a function of time. For isotropic flows, results suggest that helicity increases turbulent diffusion (when compared with nonhelical flows), in good agreement with previous studies and theoretical predictions [19,20]. In the presence of rotation, the overall effect of rotation (irrespectively of the content of helicity of the flow) is to decrease horizontal diffusion, while vertical diffusion remains approximately the same as in the isotropic case. Helicity further decreases horizontal diffusion, but slightly increases vertical diffusion (compared with the nonhelical rotating case). The decrease in horizontal diffusion is explained using a simple model for turbulence diffusivity based on the amplitude of the small-scale velocity fluctuations.

II. SETUP AND SIMULATIONS

A. Equations and numerical method

Data analyzed in the following sections stems from direct numerical simulations of the incompressible Navier-Stokes equations for the velocity $\mathbf{u}$ in a rotating frame, and of the advection-diffusion equation for the passive scalar θ, given by

$$\partial_t \mathbf{u} + \mathbf{u}\cdot\nabla\mathbf{u} = -2\boldsymbol{\Omega}\times\mathbf{u} - \nabla p + \nu\nabla^2\mathbf{u} + \mathbf{f}, \tag{1}$$

$$\partial_t \theta + \mathbf{u}\cdot\nabla\theta = \kappa\nabla^2\theta + \phi, \tag{2}$$

$$\nabla\cdot\mathbf{u} = 0. \tag{3}$$

Here, p is the total pressure (including centrifugal forces) divided by the mass density (with the mass density taken to be uniform in all simulations as a result of flow incompressibility), ν is the kinematic viscosity, and κ is the scalar diffusivity. Also, $\mathbf{f}$ is an external force that drives the turbulence, ϕ is the source of the scalar field, and $\boldsymbol{\Omega} = \Omega\hat{z}$ is the rotation angular velocity.

Equation (2) for the passive scalar θ is written in the rotating frame of reference, in which only the velocity field $\mathbf{u}$ is responsible for the advection (see, e.g., [12,14,24]). In the laboratory frame of reference, a rigid body rotation should be added to the velocity $\mathbf{u}$.

The total pressure p is obtained dynamically from the divergence of Eq. (1); using Eq. (3) this results in a Poisson equation

$$\nabla^2 p = -\nabla\cdot(\mathbf{u}\cdot\nabla\mathbf{u} + 2\boldsymbol{\Omega}\times\mathbf{u}). \tag{4}$$

Note that as in the rotating frame of reference this equation does not depend explicitly on the spatial coordinates, it is a common practice to study homogeneous rotating turbulence in incompressible fluids using periodic boundary conditions [22,25–30], for which powerful numerical methods are available.

To solve Eqs. (1) and (2), we thus use a parallel pseudospectral code in a three dimensional domain of linear size 2π with periodic boundary conditions [31,32]. The pressure is obtained by solving Eq. (4) at every time step. All equations are evolved in time using a second-order Runge-Kutta method. The code uses the $\frac{2}{3}$ rule for dealiasing, and as a result the maximum resolved wave number is $k_{\max} = N/3$, where N is the number of grid points in each direction. In all cases, the simulations are well resolved, in the sense that the Kolmogorov dissipation wave numbers for the kinetic energy and passive scalar variance, respectively k_ν and k_κ, are smaller than the maximum wave number $k_{\max}$ at all times. More details of the numerical procedure can be found in [13].

B. Dimensionless numbers and parameters

We will characterize the simulations using as dimensionless numbers the Reynolds, Peclèt, and Rossby numbers, defined as usual respectively as

$$\mathrm{Re} = \frac{UL}{\nu}, \tag{5}$$

$$\mathrm{Pe} = \frac{\nu}{\kappa}\mathrm{Re}, \tag{6}$$

$$\mathrm{Ro} = \frac{U}{2L\Omega}, \tag{7}$$

where U is the rms velocity, and L is the forcing scale of the flow defined as $2\pi/k_F$ with k_F the forcing wave number. In all simulations, U is close to unity in the turbulent steady state, and the kinematic viscosity is $\nu = 6\times10^{-4}$. The molecular scalar diffusivity is set equal to the kinematic viscosity for all runs, resulting in $\mathrm{Pe} = \mathrm{Re}$.

C. Initial conditions and external forcing

We performed a set of nonhelical simulations and a set of helical simulations with varying Rossby numbers (see Table I). In all cases, we first conducted a simulation solving only Eqs. (1) and (3) (i.e., the incompressible Navier-Stokes equations without a passive scalar), starting from the fluid at rest ($\mathbf{u} = 0$), and applying a random isotropic external mechanical forcing $\mathbf{f}$ to reach a turbulent steady state. This turbulent steady state was integrated for at least 13 turnover times. The mechanical forcing $\mathbf{f}$ used to sustain the turbulent velocity field was a superposition of Fourier modes with random phases, delta-correlated in time, with tunable injection of helicity using the methods described in Ref. [33]. Briefly, to control the total amount of helicity in the forcing, two random

TABLE I. Parameters used for the simulations: k_F is the forcing wave number, Ω is the rotation rate, Ro is the Rossby number, ν is the kinematic viscosity, Re is the Reynolds number, and $H = \langle\mathbf{u}\cdot\nabla\times\mathbf{u}\rangle$ is the mean helicity. Note that runs labeled with "A" have helicity fluctuating around zero, while runs labeled with "B" have nonzero helicity.

Run	k_F	Ω	Ro	ν	Re	H
A1	2	0	∞	6×10^{-4}	525	0
A2	2	8	0.02	6×10^{-4}	525	0
A3	2	16	0.01	6×10^{-4}	525	0
B1	2	0	∞	6×10^{-4}	525	≈2
B2	2	8	0.02	6×10^{-4}	525	≈2
B3	2	16	0.01	6×10^{-4}	525	≈2

fields are generated in Fourier space at each time step

$$v_j^{(1)}(\mathbf{k}) = A(|\mathbf{k}|)e^{i\phi_j}, \quad v_j^{(2)}(\mathbf{k}) = A(|\mathbf{k}|)e^{i\psi_j}, \tag{8}$$

where $j = 1,2,3$ are the Cartesian components of the fields, $\phi_j(\mathbf{k})$ and $\psi_j(\mathbf{k})$ are random phases, and $A(k)$ (with $k = |\mathbf{k}|$) is a real amplitude used to control the isotropic spectrum of the forcing (in our case, a narrow function centered around k_F). Two normalized and incompressible fields are then constructed as

$$\mathbf{f}^{(1)} = \frac{\nabla \times \mathbf{v}^{(1)}}{\langle|\nabla \times \mathbf{v}^{(1)}|^2\rangle^{1/2}}, \quad \mathbf{f}^{(2)} = \frac{\nabla \times \mathbf{v}^{(2)}}{\langle|\nabla \times \mathbf{v}^{(2)}|^2\rangle^{1/2}}. \tag{9}$$

We finally correlate these two incompressible random fields to build a forcing with helicity. We compute $\omega_f = \nabla \times [\sin(\alpha)\mathbf{f}^{(1)} + \cos(\alpha)\mathbf{f}^{(2)}]$, where $\alpha \in [0,\pi/4]$ is a free parameter that controls how helical the forcing is. Then, we build the forcing function as

$$\mathbf{f}(\mathbf{k}) = f_0\left[\cos(\alpha)\mathbf{f}^{(1)}(\mathbf{k}) + \sin(\alpha)\mathbf{f}^{(2)}(\mathbf{k}) + \frac{\omega_f(\mathbf{k})}{k}\right], \tag{10}$$

where f_0 is the global amplitude of the forcing. The amount of helicity in the forcing is then proportional to $\sin(2\alpha)$, which results in zero helicity for $\alpha = 0$, and maximum helicity for $\alpha = \pi/4$.

The procedure described above resulted in several runs as listed in Table I, with runs named with the letter "A" corresponding to simulations for wich the forcing injected zero mean helicity, and runs labeled as "B" corresponding to runs with maximal injection of helicity. The final state of the velocity field in the turbulent steady state of these runs was used as initial condition for multiple runs in which the external mechanical forcing $\mathbf{f}$ was maintained, but a passive scalar was injected either as an initial concentration $\theta(t = 0,\mathbf{x})$, or randomly injected in time using the source ϕ.

These two different ways to inject the passive scalar depended on the properties of the scalar that were studied. To characterize scaling laws and intermittency of the passive scalar in rotating helical and nonhelical flows, the source term ϕ was used to reach a turbulent steady state in the variance of the scalar as well as in the kinetic energy. To this end, the source ϕ was chosen as a superposition of Fourier modes with random phases, delta-correlated in time, injected at the same wave numbers k_F used in the mechanical forcing $\mathbf{f}$.

Instead, to study passive scalar turbulent diffusion, and to compute effective transport coefficients, we turned off the source term in Eq. (2) (i.e., we set $\phi = 0$). We then imposed two different initial conditions for the passive scalar, and integrated the velocity field and the passive scalar from those conditions to characterize horizontal and vertical diffusion. In each case, we used as initial condition Gaussian profiles as follows:

$$\theta(t = 0,x_i) = \theta_0 e^{-(x_i-\mu)^2/\sigma^2}, \tag{11}$$

where $i = 1$ or 3 (i.e., the initial profile can be a function solely of $x_1 = x$, or solely of $x_3 = z$), $\mu = \pi$ (the profile is centered in the middle of the box, with the box of length 2π), and $\sigma = 1$. When $x_1 = x$ is used, this allows us to study the diffusion of the initial profile in the direction perpendicular to rotation (or "horizontal"), while when $x_3 = z$ is used, we study diffusion in the direction parallel to rotation (or "vertical"). For all runs, we also verified explicitly that the diffusion in the x and y directions was the same (to be expected as rotating flows tend to be axisymmetric). These runs with no source term ϕ and with Gaussian initial profiles for the scalar will be labeled with a subindex indicating the dependence of the initial profile (e.g., runs labeled $A1_x$ or $A1_z$ indicate the run A1 was continued with an initial Gaussian profile for θ that depends, respectively, on x or on z).

III. TURBULENT SCALING LAWS

In this section, we present numerical results for the energy and passive scalar spectra, structure functions, and PDFs for helical and nonhelical rotating flows. To get the results in this section, the simulations in Table I were continued forcing the velocity and the passive scalar to reach a turbulent steady state in both quantities. We first present the methods used to analyze the data, then present the results for the spectra and inertial range scaling laws, and finally we characterize intermittency using structure functions and PDFs. We also compare the data with predictions from a simple phenomenological model, with Kraichnan model for the passive scalar, and with a multifractal model.

A. Methods

In this first part of the paper, the analysis consists on the characterization of flow anisotropy, scaling laws, and intermittency. To this end, we consider power spectra, structure functions, and PDFs of passive scalar and velocity field increments for all runs.

As a result of the anisotropy introduced by rotation, we consider reduced perpendicular energy and passive scalar spectra, namely $E(k_\perp)$ and $V(k_\perp)$. These reduced spectra are defined by summing the power of all (velocity or passive scalar) modes in Fourier space over cylindrical shells with radius $k_\perp$, with their axis aligned with the direction of the rotation axis.

To compute structure functions and PDFs, field increments must be defined first. Given the preferred direction introduced by rotation, it is natural to consider an axisymmetric decomposition for the increments. In general, the longitudinal increments of the velocity and the increments of the passive scalar fields are defined, respectively, as

$$\delta u(\mathbf{x},\mathbf{l}) = [\mathbf{u}(\mathbf{x}+\mathbf{l}) - \mathbf{u}(\mathbf{x})] \cdot \frac{\mathbf{l}}{|\mathbf{l}|}, \tag{12}$$

$$\delta\theta(\mathbf{x},\mathbf{l}) = \theta(\mathbf{x}+\mathbf{l}) - \theta(\mathbf{x}), \tag{13}$$

where the increment $\mathbf{l}$ can point in any direction. Structure functions of order p are then defined as

$$S_p(\mathbf{l}) = \langle|\delta u(\mathbf{x},\mathbf{l})|^p\rangle \tag{14}$$

for the velocity field, and as

$$T_p(\mathbf{l}) = \langle|\delta\theta(\mathbf{x},\mathbf{l})|^p\rangle \tag{15}$$

for the passive scalar field. Here, angular brackets denote spatial average over all values of $\mathbf{x}$.

These structure functions depend on the direction of the increment (i.e., they do not assume any symmetry in the

flow). In simulations without rotation, the field is isotropic and the SO(3) decomposition is used to calculate the isotropic component of the structure functions [34–36]. In the rotating case, due to the axisymmetry of the flow, we will consider only increments perpendicular to $\hat{z}$ (the rotation axis), and increments parallel to $\hat{z}$. We denote the former increments using $l_\perp$, the latter with $l_\parallel$, and we follow the procedure explained in detail in [13,37] to average over several $l_\perp$ directions.

This procedure to average Eqs. (14) and (15) over several directions can be summarized as follows. Velocity and passive scalar structure functions are computed from Eqs. (12) and (13) using 26 different directions for the increments $\mathbf{l}$, generated by integer multiples of the vectors (1,0,0), (1,1,0), (2,1,0), (3,1,0), (0,1,0), (−1,1,0), (−1,2,0), (−2,1,0), (−1,2,0), (−1,3,0), (−3,1,0), (−1,3,0) (all vectors are in units of grid points in the simulations), the 13 vectors obtained by multiplying them by −1, and the two vectors (0,0,±1) for the translations in z. Once all structure functions were calculated, the perpendicular structure functions $S_p(l_\perp)$ and $T_p(l_\perp)$ are obtained by averaging over the 24 directions in the $x-y$ plane, and the parallel structure functions $S_p(l_\parallel)$ and $T_p(l_\parallel)$ can be computed directly using the generators in the z direction.

For all runs, this procedure was applied to N_s snapshots of the velocity and of the passive scalar fields, separated by at least one turnover time each. For large enough Reynolds number, the structure functions are expected to show inertial range scaling, i.e., we expect that for some range of scales $S_p \sim l_\perp^{\xi_p}$ and $T_p \sim l_\perp^{\zeta_p}$, where ξ_p and ζ_p are, respectively, the scaling exponents of order p of the velocity and scalar fields. Scaling exponents shown below are calculated for all the snapshots analyzed in each simulation, and averaged over time. Errors are then defined as the mean square error; e.g., for the passive scalar exponents, the error is

$$e_{\zeta_p} = \frac{1}{N_s}\sqrt{\sum_{i=1}^{N_s}\left(\zeta_{p_i} - \overline{\zeta_p}\right)^2}, \tag{16}$$

where ζ_{p_i} is the slope obtained from a least square fit for the ith snapshot, and $\overline{\zeta_p}$ is the mean value averaged over all snapshots. The error in the least square calculation of the slope for each snapshot is much smaller than this mean square error and neglected in the propagation of errors. Extended self-similarity (ESS) [38,39] is not used to obtain the scaling exponents, except when explicitly stated.

B. Energy and passive scalar spectra

In the presence of rotation and in the absence of helicity, the spectral behavior of the passive scalar is strongly anisotropic and quasi-two-dimensional [13]. As previously shown in [13], $E(k_\perp) \sim k_\perp^{-2}$ for the velocity field and $V(k_\perp) \sim k_\perp^{-3/2}$ for the passive scalar. The presence of helicity in rotating flows affects the cascade of energy and of the passive scalar to smaller scales. Numerical simulations in [22] showed that, when helicity is present in rotating flows, the direct cascade of helicity dominates over the direct cascade of energy in the inertial range. This is the result of the development of an inverse cascade of energy, which leaves less energy available for the system to transfer to small scales. Assuming the direct cascade of helicity is dominant, the direct flux of helicity δ in the inertial range can be estimated as

$$\delta \sim \left(\frac{h_{l_\perp}}{\tau_{l_\perp}}\right)\left(\frac{\tau_\Omega}{\tau_{l_\perp}}\right), \tag{17}$$

where $h_{l_\perp}$ is the characteristic helicity at scale $l_\perp$, $\tau_{l_\perp} \sim l_\perp/u_{l_\perp}$ is the eddy turnover time at that scale (with $u_{l_\perp}$ the characteristic velocity), and $\tau_\Omega \sim 1/\Omega$ is the rotation period. The factor $\tau_\Omega/\tau_{l_\perp}$ on the right accounts for the slowdown of the transfer to small scales due to the nonlinear interaction of inertial waves in the presence of rotation (see, e.g., [40–42]). For a helicity spectrum $H(k_\perp) \sim h_{l_\perp}/k_\perp$, and for an energy spectrum $E(k_\perp) \sim u_{l_\perp}^2/k_\perp$, it follows from Eq. (17) that $E(k_\perp)H(k_\perp) \sim \delta\Omega k_\perp^{-4}$ (see [22,43]). In other words, if the energy spectrum satisfies $E(k_\perp) \sim k_\perp^{-n}$, then the helicity must follow a spectrum $H(k_\perp) \sim k_\perp^{4-n}$. It follows from Schwarz's inequality that $|H(k)| \leqslant kE(k)$. As a result, the energy spectrum becomes steeper as the flow becomes more helical, with the limit of a spectral index $n = 2.5$ for the energy in the case of a turbulent flow with maximum helicity, for which $|H(k)| = kE(k)$. In practice, this limit cannot be attained since in a flow with maximum helicity the nonlinear term becomes negligible, resulting in no net energy transfer (see [43] for details).

Figure 1 shows compensated energy and passive scalar reduced perpendicular spectra for runs A3 and B3 (both runs with rotation, and respectively without and with net helicity). The compensated isotropic spectra for run A1 (without rotation) are also shown as references. In the rotating cases, the kinetic energy spectrum is steeper in the presence of helicity, compatible with $E(k_\perp) \sim k_\perp^{-2.2}$ scaling, while the passive scalar is close to $V(k_\perp) \sim k_\perp^{-1.4}$ scaling. Although resolution is moderate in these simulations (see [13] for more detailed studies of spectral scaling), the scaling laws can be further confirmed in Fig. 2, where a detail of the compensated energy and passive scalar spectra for run B3 are shown. In Fig. 2 we also present the helicity spectrum compensated by $k_\perp^{-1.8}$ (to confirm that the helicity spectral index and energy spectral index add to 4). Similar scaling laws were observed in the rest of the helical rotating runs listed in Table I.

In [13] we presented a phenomenological argument to predict the scaling of the passive scalar spectrum in the presence of rotation, inspired in the classical Kolmogorov-Obukhov scaling for isotropic and homogeneous turbulence. Using this argument, we can explain the effect of helicity in the scaling of the passive scalar spectrum. From Eq. (2), the passive scalar flux σ can be estimated as

$$\sigma \sim \frac{\theta_{l_\perp}^2}{\tau_{l_\perp}} \sim \frac{\theta_{l_\perp}^2 u_{l_\perp}}{l_\perp}. \tag{18}$$

Note that the passive scalar flux is not affected directly by rotation, as Ω does not appear explicitly in Eq. (2). However, the scaling of the passive scalar will be affected by changes in the scaling of the velocity field, which depend on rotation. If we assume that the passive scalar has a direct cascade with constant flux σ in the inertial range, then the passive scalar power spectrum $V(k_\perp) \sim \theta_{l_\perp}^2/k_\perp$ can be estimated,

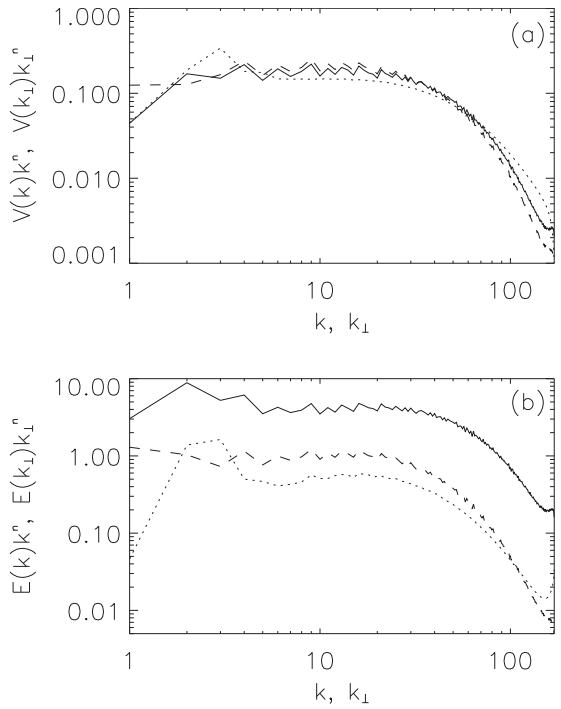

FIG. 1. (a) Reduced perpendicular passive scalar variance spectra $V(k_\perp)$, compensated by $k_\perp^{-n}$. The solid line corresponds to run B3 (rotating and helical) with $n = 1.4$, and the dashed line corresponds to run A3 (rotating and nonhelical) with $n = 1.5$. As a reference, the compensated isotropic spectrum $V(k)k^n$ for run A1 (no rotation) with $n = \frac{5}{3}$ is shown by the dotted line. (b) Same for the reduced perpendicular energy spectrum $E(k_\perp)$. The solid line corresponds to run B3 with $n = 2.2$ and the dashed line corresponds to run A3 with $n = 1.5$. The dotted line corresponds to the compensated isotropic spectrum $E(k)k^n$ for run A1 with $n = \frac{5}{3}$. Note the bottleneck in the energy spectrum of the simulation without rotation. All the spectra are averaged in time.

using Eq. (18), as

$$V(k_\perp) \sim \frac{\sigma l_\perp^2}{u_{l_\perp}}. \tag{19}$$

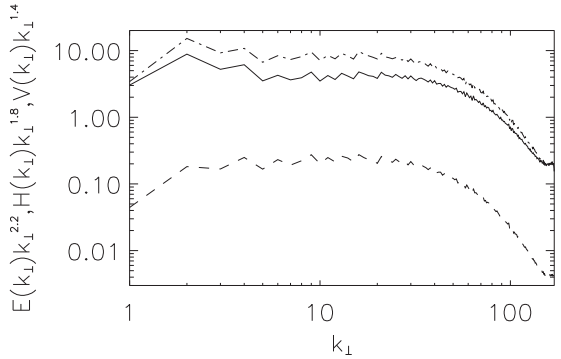

FIG. 2. Reduced perpendicular energy spectrum compensated by $k_\perp^{-2.2}$ (solid line), reduced perpendicular passive scalar spectrum compensated by $k_\perp^{-1.4}$ (dashed line), and reduced perpendicular helicity spectrum compensated by $k_\perp^{-1.8}$ (dashed-dotted line) in run B3 (with rotation and helicity).

For an energy spectrum $E(k_\perp) \sim k_\perp^{-n}$, and therefore for a characteristic velocity at scale l satisfying $u_{l_\perp} \sim l_\perp^{1-n}$, the passive scalar spectrum in Eq. (19) results

$$V(k_\perp) \sim \sigma l_\perp^{\frac{5-n}{2}} \sim \sigma k_\perp^{-\frac{5-n}{2}}. \tag{20}$$

Therefore, the spectral index for the passive scalar inertial range is

$$n_\theta = \frac{5-n}{2}. \tag{21}$$

This relation was shown in [13] to be compatible with the scaling law followed by the passive scalar spectrum in numerical simulations of nonhelical flows in the presence of rotation. Here, we confirm that this argument remains valid in the presence of helicity in the rotating flow. Moreover, when rotation is zero, we recover $n_\theta = \frac{5}{3}$, in good agreement with the Kolmogorov scaling previously observed for passive scalars in isotropic turbulence (see, e.g., [2]).

C. Structure functions and scaling exponents

Structure functions and scaling exponents for the passive scalar in nonhelical rotating flows were studied in detail in [13]. As a result, here we focus on the simulations with helical forcing. Figure 3 shows the axisymmetric and perpendicular (i.e., only for perpendicular increments $l_\perp$) structure functions for the passive scalar and for the velocity field up to seventh order for run B3. Each curve corresponds to an average over $N_s = 8$ snapshots of the turbulent steady state of the simulation. The structure functions show a range of scales

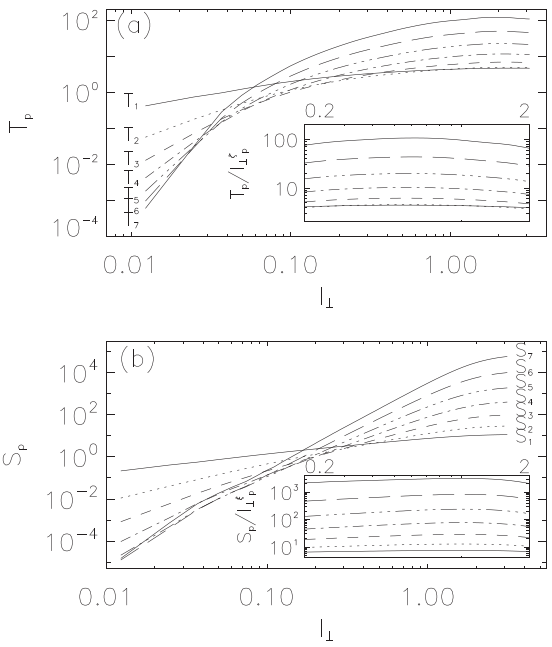

FIG. 3. Averaged axisymmetric structure functions (only for $l_\perp$ increments) up to seventh order in run B3 (rotating and helical) for (a) the passive scalar and (b) the velocity field. The insets show the structure functions in the inertial range, compensated (a) by $l_\perp^{\zeta_p}$ and (b) by $l_\perp^{\xi_p}$, where ζ_p and ξ_p are, respectively, the scaling exponents of the passive scalar and of the velocity field.

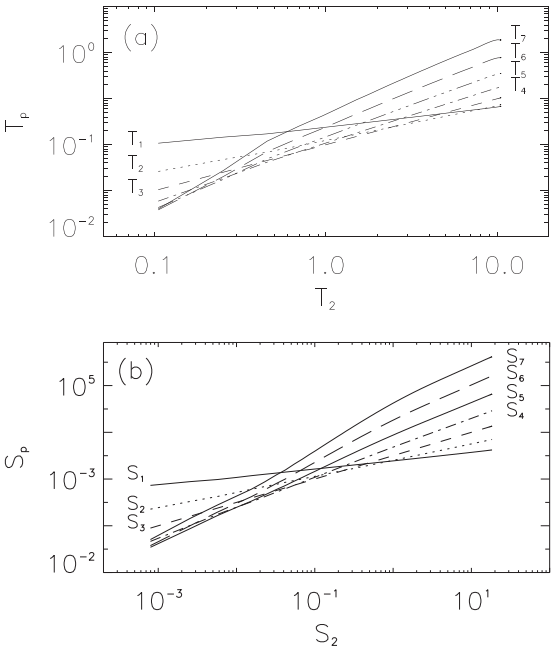

FIG. 4. Averaged axisymmetric structure functions using ESS (only for $l_\perp$ increments) up to seventh order in run B3 (rotating and helical) for (a) the passive scalar and (b) the velocity field.

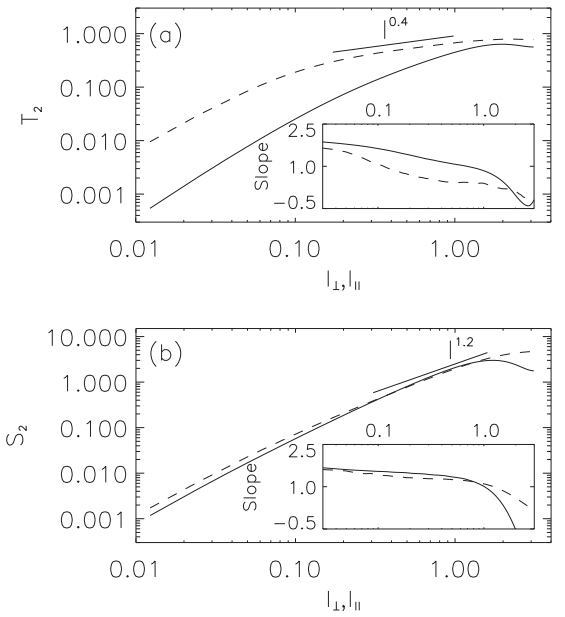

FIG. 5. Axisymmetric second-order structure functions for run B3 (helical with rotation) for (a) the passive scalar and (b) the velocity field. In both panels, solid lines correspond to the parallel structure functions, while dashed lines correspond to the perpendicular structure functions. Slopes indicated as references correspond to the time average of the scaling exponents, obtained from a best fit in the inertial range of the structure functions at different times. The insets show the local slope of the structure functions, obtained independently from a computation of the local derivative. Note that while perpendicular structure functions (dashed lines) show a narrow range of scales with approximately constant slope, the parallel structure functions (solid lines) decrease rapidly.

with approximately power-law scaling at intermediate scales (see the insets in Fig. 3), while at the smallest scales approach the $\sim l^p$ scaling expected for a smooth field in the dissipative range.

As the inertial range observed in Fig. 3 is rather narrow (specially for the highest orders considered), Fig. 4 shows the same structure functions as in Fig. 3, for the velocity field and for the passive scalar, but using the ESS hypothesis [38]. When using ESS, the structure functions are plotted as a function of the second-order structure function of the same field, which results in an extended range of scales with power-law scaling. This is the case in our simulations except at small scales and for the highest order considered. Thus, we will consider below the scaling exponents up to seventh order for all simulations, keeping in mind that for this order convergence is not as good as for the other orders.

Figure 5 shows a detail for run B3 of the passive scalar and velocity field second-order perpendicular structure functions, respectively $T_2(l_\perp)$ and $S_2(l_\perp)$, as well as the structure functions for increments parallel to the rotation axis $T_2(l_\parallel)$ and $S_2(l_\parallel)$. Stronger anisotropy is observed at small scales for the passive scalar than for the velocity field, manifested as a larger difference between $T_2(l_\parallel)$ and $T_2(l_\perp)$ than between $S_2(l_\parallel)$ and $S_2(l_\perp)$. Also, an inertial range with power-law scaling can be identified at intermediate scales in $T_2(l_\perp)$ and $S_2(l_\perp)$. The range of scales is consistent with the wave numbers of the inertial range in the corresponding spectra. The slopes indicated as a reference in Fig. 5 correspond to the time average of the second-order scaling exponents, obtained from a best fit in the inertial range of all structure functions at different times (the insets in Fig. 5 also show an estimation of the slope based on the local derivative of the structure functions). From the best fit, the second-order scaling exponents (in the perpendicular direction) are $\zeta_2 = 0.41 \pm 0.01$ for the passive scalar and $\xi_2 = 1.22 \pm 0.01$ for the velocity field. These values are in good agreement with the spectra $V(k_\perp) \sim k^{1.4}$ and $E(k_\perp) \sim k^{2.2}$, which from dimensional analysis lead to $T_2(l_\perp) \sim l_\perp^{0.4}$ and $S_2(l_\perp) \sim l_\perp^{1.2}$.

From the curves in Fig. 3 or in Fig. 4, scaling exponents can also be computed for lower and higher orders. As mentioned above, based on the amount of statistics available, velocity and passive scalar exponents in the direct cascade range were computed for all runs up to the seventh order. We also compared the resulting exponents when using (or not) the ESS hypothesis (i.e., using, as an example for run B3, the data displayed, respectively, in Figs. 3 or 4), obtaining consistent results in all cases. Thus, we present below only the scaling exponents without ESS.

Figure 6 shows the resulting velocity scaling exponents ξ_p and passive scalar exponents ζ_p for runs B2 and B3 (both helical, with $\mathrm{Ro} = 0.02$ and 0.01, respectively). The scaling exponents for the case without rotation and without helicity (run A1) are also shown for comparison. Linear (nonintermittent) scalings for ζ_p and for ξ_p are shown as a reference as well, based on the values of the second-order exponents ζ_2 and ξ_2 for runs B2 and B3. Finally, and as a reference, in Fig. 6 we also show the the prediction of the Kraichnan model [3], which is a model for the advection and diffusion of a passive scalar in a random, delta-correlated in

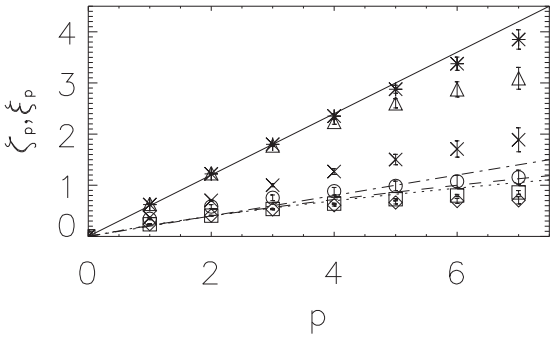

FIG. 6. Scaling exponents (with error bars) as a function of the order p in simulations of helical rotating turbulence, for the velocity field (triangles for run B2 and stars for run B3, both with helicity and with decreasing Rossby number), and for the passive scalar (diamonds for run B2 and squares for run B3). The solid line corresponds to the linear scaling expected for the velocity field exponents in the absence of intermittency, while the dashed-dotted line corresponds to nonintermittent scaling for the passive scalar exponents. The dotted and dashed lines correspond to Kraichnan's model with $\zeta_2 = 0.4$ and, respectively, with $d = 2$ and 3. As a reference, we also show the scaling exponents for the simulation A1 (without rotation, i.e., for isotropic and homogeneous turbulence): crosses correspond to the velocity field exponents, and circles to the passive scalar exponents.

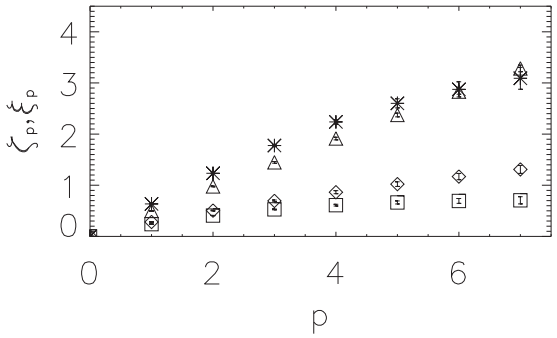

FIG. 7. Scaling exponents (with error bars) as a function of the order p in simulations of rotating turbulence with and without helicity, for the velocity (triangles for run A3 without helicity and stars for run B3 with helicity) and for the passive scalar (diamonds for run A3 and squares for run B3).

time velocity field in a space with dimensionality d (another model is presented below). The scaling exponents for the passive scalar in the Kraichnan model are

$$\zeta_p = \tfrac{1}{2}[\sqrt{2d\zeta_2 p + (d-\zeta_2)^2} + (d-\zeta_2)]. \qquad (22)$$

For the curves in Fig. 5, these exponents were evaluated with the value of ζ_2 obtained from the simulations, and using either $d = 2$ or 3.

Scaling exponents for the velocity field are similar up to $p = 4$ in both runs with rotation. The second-order velocity field exponent is $\xi_2 = 1.22 \pm 0.02$ for run B2 and $\xi_2 = 1.23 \pm 0.01$ for run B3. The velocity field exponents display the well-known deviations from linear scaling associated with intermittency, more evident for the higher order exponents and in the simulation with larger Rossby number (i.e., smaller rotation rate). The deviation from strict scale invariance is often quantified in terms of the intermittency exponent $\mu = 2\xi_3 - \xi_6$, which for these runs is $\mu = 0.6 \pm 0.2$ for run B2 and $\mu = 0.2 \pm 0.1$ for run B3. The decrease in the values of μ suggest a reduction of intermittency with increasing rotation, as observed before in simulations and in experiments [13,29,37,44–47].

The passive scalar exponents for these two runs also display similar values. The second-order scaling exponent is $\zeta_2 = 0.41 \pm 0.01$ for both runs. Deviations from linear scaling are observed, and the intermittency exponents are $\mu_s = 0.36 \pm 0.06$ for run B2 and $\mu_s = 0.27 \pm 0.04$ for run B3. For runs B2 and B3, Kraichnan's model adjusts the numerical data best with $\zeta_2 = 0.4$ and $d = 2$. The value of d is compatible with quasibidimensionalization in the spatial distribution of the passive scalar in the presence of rotation, as reported in the presence of rotation in [13] (see also a recent study of bidimensionalization of rotating turbulence in [48]). However, it may also be the case that the exponents for the passive scalar deviate from Kraichnan's model for $d = 3$ as the velocity field in the numerical simulations is intermittent, affecting the scalar statistics, while Kraichnan's model assumes a random nonintermittent velocity. To gain a better understanding of the multifractal properties of the passive scalar distribution, we thus derive another intermittency model in the next subsection.

Overall, the decrease in the values of μ observed for both the velocity field and the passive scalar indicate a reduction of intermittency with decreasing Rossby number. However, this reduction is significantly more pronounced for the velocity field than for the passive scalar. In Fig. 6, note intermittency is not necessarily associated with how small the scaling exponents are for large values of p, but rather with how much the exponents deviate from a straight line that goes through the $p = 2$ scaling exponent. This is evident for the velocity field exponents ξ_p, but less evident for the passive scalar exponents ζ_p.

Finally, we present a comparison between the scaling exponents in rotating turbulence with and without helicity. Figure 7 shows the velocity field and passive scalar exponents for runs A3 and B3 (respectively without and with helicity). In this case, deviations from linear (nonintermittent) scaling are clearly larger for the passive scalar in B3, indicating stronger intermittency in the presence of helicity.

D. Multifractal model for the passive scalar

In recent years, a number of models have been proposed to consider intermittency corrections to velocity and passive scalar exponents (see, e.g., [49,50]). In these models, corrections to the linear (nonintermittent) scaling exponents result from the consideration that the fields are defined over a fractal or a multifractal set (i.e., that the structures in the inertial range are not space filling). This in turn follows from the consideration that the cascade (and thus local dissipation) has fractal or multifractal distribution, or from assumptions on the underlying probability distribution of the local flux of energy and of passive scalar variance towards smaller scales.

While the Kraichnan model [3] is important as it was derived exactly from the passive scalar equation for a simple (and nonintermittent) velocity field, these multifractal models can give a better fit to the data, and provide complementary

information on the geometrical properties of the inertial range structures, and of how much space filling are these structures [51]. One of the most successful of these models is that of She and Leveque [49], which has been extended to the case of passive scalars in isotropic and homogeneous turbulence [50]. We thus take this latter model as a motivation to derive a multifractal model for the passive scalar in the presence of rotation.

Following their approach, we assume that the locally averaged (on a scale $l_\perp$) passive scalar dissipation rate σ_l results from a hierarchy of fluctuating structures with scaling

$$\langle \sigma_{l_\perp}^p \rangle \sim l_\perp^{\tau_p}. \tag{23}$$

Note that we are using $l_\perp$ as we assume the scaling is anisotropic in the presence of rotation, and that in the turbulent steady state σ_l is also a proxy for the locally averaged scalar flux.

From the Monin and Yaglom result [52], or equivalently from the locally averaged Eq. (18), we can write

$$\langle \delta\theta_{l_\perp}^2 \delta u_{l_\perp} \rangle \sim \sigma_{l_\perp} l_\perp, \tag{24}$$

which can be easily rewritten as a relation between the passive scalar exponents ζ_p, the velocity scaling exponents ξ_p, and the exponents τ_p as

$$\zeta_p = \frac{p}{2} + \tau_{p/2} - \xi_{p/2}. \tag{25}$$

As shown in Fig. 6, intermittency of the velocity field in the rotating case is very weak. We can thus neglect intermittency corrections in ξ_p and simplify this latter equation using $\xi_p = \alpha p$ (i.e., linear dependence of the exponents), where α is a constant to be determined from the kinetic energy spectrum. For inertial range scales $E(k_\perp) \sim k_\perp^{-n}$ and thus $\langle \delta u_{l_\perp}^p \rangle \sim l_\perp^{(n-1)/2}$, which results in $\alpha = (n-1)/2$. Replacing in Eq. (25), the passive scalar exponents of order p can be written as

$$\zeta_p = \frac{(3-n)}{4} p + \tau_{p/2}. \tag{26}$$

As in the She-Leveque model for the velocity field in isotropic and homogeneous turbulence, the exponents τ_p can be estimated using geometrical arguments. She and Leveque assumed a scaling law for successive powers of the dissipation at scale l. For the passive scalar dissipation, this assumption corresponds to the relation

$$\sigma_{l_\perp}^{(p+1)} \sim \left(\sigma_{l_\perp}^{(p)}\right)^\beta \left(\sigma_{l_\perp}^{(\infty)}\right)^{\beta-1}, \tag{27}$$

where $\sigma_{l_\perp}^{(p)} = \langle \sigma_{l_\perp}^{p+1} \rangle / \langle \sigma_{l_\perp}^p \rangle$. Here, $\sigma_{l_\perp}^{(\infty)} \sim \theta^2 / t_{l_\perp}$ is the maximum variance of the scalar that can be dissipated by the most intermittent structures in a time $t_{l_\perp}$. As in the She-Leveque model, we can assume that the mixing rate of fluid elements that determine the time scale for the dissipation is homogeneous in space, and simply write $t_{l_\perp} \approx l_\perp^x$ where x is a parameter of the system to be determined later. Introducing the codimension of the intermittent structures $C_0 = d - D$ (with d the space dimensionality as before, and D the fractal dimension of the structures), standard She-Leveque phenomenology then leads to [49,50]

$$\tau_p = -xp + C_0(1 - \beta^p). \tag{28}$$

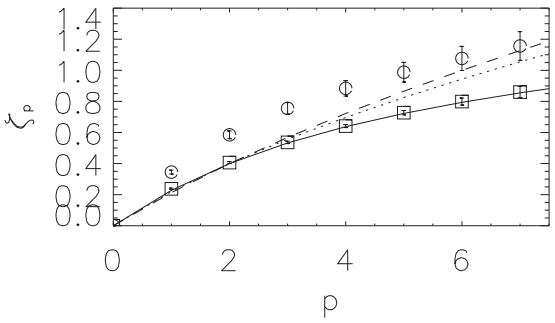

FIG. 8. Passive scalar scaling exponents with error bars for runs A1 (circles, isotropic and homogeneous turbulence) and B3 (squares, rotating helical turbulence). The full line represents the multifractal model from Eq. (29), and for parameters for run B3 (helical). The Kraichnan model with $\zeta_2 = 0.4$ and using $d = 2$ (dashed line) and $d = 3$ (dotted line) are also shown for comparison.

In this last expression, we already imposed the condition $\tau_0 = 0$, to have $\zeta_0 = 0$ in Eq. (26). From the condition $\tau_1 = 0$, which follows from asking ζ_2 to be compatible with the slope of the spectrum of the passive scalar variance, we obtain $C_0 = x/(1-\beta)$. Thus, Eq. (26) finally takes the form

$$\zeta_p = \frac{(3-n-2x)}{4} p + C_0(1 - \beta^{p/2}), \tag{29}$$

which has only two free parameters, x and C_0, which can be associated with geometrical properties of the structures of the passive scalar in the inertial range. In [50] it was argued that the codimension of the passive scalar C_0 should be between 0.75 and 1, as the scalar tends to create sharp fronts ($C_0 = 1$ corresponds to surfacelike structures). Other authors have found $C_0 \approx 0.6$ [53]. As will be shown below, this expression adjusts well our data with $C_0 = 0.65$, which indicates strong gradients of the passive scalar takes place in spatial regions similar to those observed in isotropic and homogeneous turbulence. This will be later confirmed by spatial exploration of the passive scalar concentration, where we will also see that these regions tend to be aligned with the axis of rotation.

Simulations with and without helicity differ in the spectral scaling of the velocity field, and thus on the value of n in Eq. (29). The multifractal model is in good agreement with the exponents of all rotating cases as long as n is varied following the kinetic energy spectrum of each simulation. As we are mostly interested in the helical case here, Fig. 8 shows the passive scalar scaling exponents for run B3 (rotating and helical, with $n = 2.2$ as obtained from the kinetic energy spectrum), and the exponents obtained from Eq. (29) with $x = 0.32$. As a reference, we also show the exponents obtained from Kraichnan's model, and the scaling exponents in the simulation without helicity nor rotation (run A1). As mentioned above, the value of x in the multifractal model is associated with the scaling of the most dissipative structures. In isotropic and homogeneous turbulence $x \approx \frac{2}{3}$ for both the velocity and the passive scalar [49,50], while in magnetohydrodynamics the magnetic field (which is more intermittent) has $x \approx \frac{1}{2}$ [54]. The value found here is $x \approx \frac{1}{3}$ and is in agreement with an even more intermittent distribution of the scalar field.

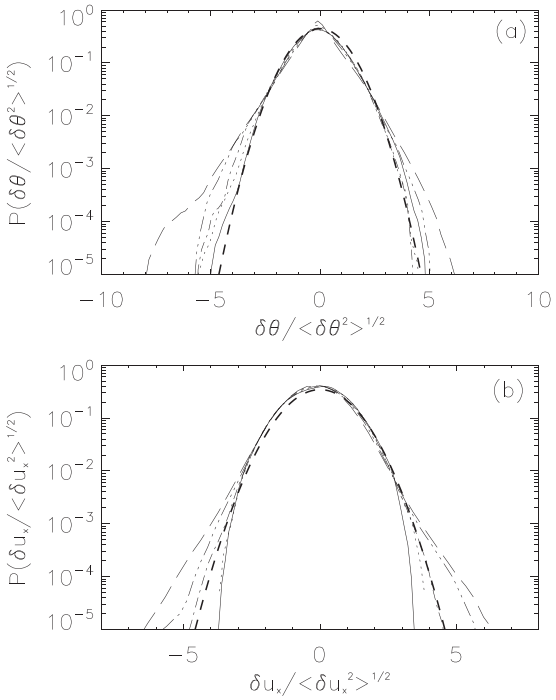

FIG. 9. Probability density functions in run B3, for five different horizontal spatial increments $l = 1.6$ (solid line), 0.8 (dashed line), 0.4 (dashed-dotted line), 0.2 (dashed-triple-dotted line), and 0.1 (long dashes), and for (a) the passive scalar, and (b) the x component of the velocity field. A Gaussian curve with unit variance is indicated by the dotted curve. As intervals are decreased, curves depart more and more from the Gaussian distribution developing stronger tails.

E. Probability density functions

Intermittency and small-scale anisotropy can be also studied considering the PDFs of the field increments. In this section, we briefly discuss the PDFs of longitudinal increments of the x component of the velocity field, as well as increments and spatial derivatives of the passive scalar concentration. Quantities shown are normalized by their variance, and a Gaussian curve with unit variance is shown as a reference.

Figure 9 shows the PDFs of the velocity and of the passive scalar increments for four different values of the spatial increment ($l = 1.6$, 0.8, 0.4, 0.2, and 0.1) in run B3 (with helicity). All the increments were considered in the x direction (perpendicular to the axis of rotation), and for the velocity the x component was used to build longitudinal increments. As a reference, and to compare with the values of the increments considered, the forcing scale in this runs is $\approx\pi$, and the dissipative scale is ≈ 0.05. Therefore, increments $l = 0.8$ and 0.4 correspond to scales in the inertial range. The PDFs of velocity and passive scalar increments for $l = 1.6$ are close to Gaussian, while for smaller spatial increments non-Gaussian tails develop. Note also that in the PDFs of passive scalar increments, a strong asymmetry develops for $l = 0.4$, 0.2, and 0.1.

IV. TURBULENT DIFFUSION

In this second part of the paper, the aim is to characterize the turbulent diffusion of the passive scalar in rotating helical turbulence, and to compare it with turbulent diffusion in nonhelical rotating turbulence, as well as with turbulent diffusion in isotropic turbulence. To this end, we simulate the flows starting from an initial Gaussian profile for the concentration of the passive scalar, and we let it diffuse in directions parallel and perpendicular to the rotation axis. We then quantify effective transport coefficients by measuring the time evolution of the averaged concentration, and using Fick's law.

A. Methods

Before presenting the method used to measure the turbulent diffusion, we briefly recall how the simulations were conducted for this second study. As in the previous section, simulations in group A (see Table I) correspond to simulations with zero mean helicity, while simulations in group B correspond to simulations with helical forcing and nonzero net helicity. As explained in Sec. IV A, for each run in the turbulent steady state of the velocity field, the simulation was extended twice with the same parameters and mechanical forcing, but with two different initial conditions for the passive scalar: a Gaussian profile for the concentration in the x direction (to study horizontal diffusion) and a Gaussian profile in the z direction (to study vertical diffusion). To identify these runs, an additional subindex is used in this section to differentiate between simulations with different dependence of the initial Gaussian profile. As examples, a run labeled $A1_x$ stands for a simulation with the parameters of run A1 (i.e., with zero mean helicity and no rotation) and with initial profile of the passive scalar in the x direction, while the label $B2_z$ indicates the run has helicity, rotation, and an initial dependence of the passive scalar in the z direction.

In each of these runs, we let the initial profile diffuse for several turnover times. Meanwhile, we compute and store quantities averaged over the two directions perpendicular to the direction over which the original Gaussian profile varies. In particular, we consider the averaged passive scalar concentration $\overline{\theta}$, and the spatial passive scalar flux $\overline{\theta u_i}$, where $i = 1$ or 3 depending on the initial dependence of the Gaussian profile, and where the averages denoted by the overbars are done over the two remaining Cartesian coordinates. Note the spatial flux $\overline{\theta u_i}$ represents the amount of passive scalar transported in the i direction per unit of time by the fluctuating (or turbulent) velocity since there is no mean flow in our simulations (we use delta-correlated in time random forcing); in other words, u_i is the fluctuating velocity.

Then, the pointwise effective turbulent diffusion coefficient is given by [23]

$$\mathcal{D}_i(x_i,t) = \frac{\overline{\theta u_i}}{\partial_{x_i}\overline{\theta}}. \tag{30}$$

This coefficient corresponds to how much passive scalar is transported by the fluctuating velocity per unit of variation of $\overline{\theta}$ with respect to x_i. As already mentioned, $i = 1$ stands for horizontal diffusion, while $i = 3$ stands for vertical diffusion, where the dependence on the direction of this coefficient is the result os the flow being anisotropic.

From Fick's law, the actual turbulent diffusion coefficient is the average of $\mathcal{D}_i(x_i,t)$ over the coordinate x_i, and if the

system is in a turbulent steady state, over time. From Eq. (30), we can define these averaged diffusion coefficients as follows. We can first average over the coordinate x_i to obtain a time dependent turbulent diffusion

$$\mathcal{D}_i(t) = \frac{1}{2\pi}\int_0^{2\pi} \mathcal{D}_i(x_i,t)dx_i, \tag{31}$$

and we can further average over time, to obtain the mean turbulent diffusion

$$\mathcal{D}_i = \frac{1}{T}\int_{t_0}^{t_0+T} \mathcal{D}_i(t)dt. \tag{32}$$

Here, t_0 and T are characteristic times of the flow. In practice, in our simulations the turbulent diffusion $\mathcal{D}_i(t)$ first grows in time as the initial Gaussian profile is mixed by the turbulence, then reaches an approximate steady state value for a few turnover times, and then decreases as the scalar becomes completely diluted (which happens after three or four turnover times).

B. Isotropic helical turbulence

In the absence of rotation, diffusion coefficients are expected to be isotropic, and therefore horizontal and vertical turbulent diffusion should be the same within error bars. Figure 10 shows the mean passive scalar profile $\overline{\theta}(x,t)$, the horizontal flux $\overline{\theta u_x}(x,t)$, and the pointwise value of $\mathcal{D}_x(x,t)$, at five different times for run $A1_x$ (no rotation and no net helicity).

As time evolves, the mean profile $\overline{\theta}(x,t)$ flattens and widens. The flux is antisymmetric: it is positive for $x > \pi$ and negative for $x < \pi$. This behavior for the flux is to be expected, as at $t = 0$ there is an excess of passive scalar concentration at $x = \pi$ that must be transported by turbulent diffusion towards $x = 0$ and towards $x = 2\pi$. The pointwise value of $\mathcal{D}_x(x,t)$ fluctuates around a mean value (which increases with time), except close to $x = \pi$ where it rapidly takes very large positive and negative values as in that point $\partial_x\overline{\theta}$ approaches zero. The mean spatial value of $\mathcal{D}_x(x,t)$ increases to its saturation value around $t_0 \approx 1.5$; after this time, it fluctuates around its value (see more details below).

Figure 11 shows the same quantities at five different times for run $B1_x$ (i.e., in a simulation without rotation but with injection of net helicity). The behavior of the mean concentration of the passive scalar, the horizontal scalar flux, and the pointwise value of $\mathcal{D}_x(x,t)$ is qualitatively the same as in the nonhelical run $A1_x$. However, the helical run displays a larger diffusion of the mean concentration of the scalar [as evidenced by the smaller maximum value of $\overline{\theta}(x,t)$ around $x = \pi$ and by the stronger tails close to to $x = 0$ and 2π, when curves at the same time are compared in Figs. 10 and 11]. Also, the spatial flux $\overline{\theta u_x}$ takes larger extreme values in the helical simulation, and the spatial average of $\mathcal{D}_x(x,t)$ seems to result in larger values for the turbulent diffusion in this run.

The increased turbulent diffusion in the presence of helicity is consistent with Fig. 12, which shows the horizontal turbulent diffusion as a function of time for runs $A1_x$ and $B1_x$. In both runs, $\mathcal{D}_x(t)$ grows from an initially small value to its saturation value around $t_0 \approx 1.5$. As observed above, turbulent diffusion saturates at similar times for the helical and the nonhelical cases, but to a slightly larger value in the presence

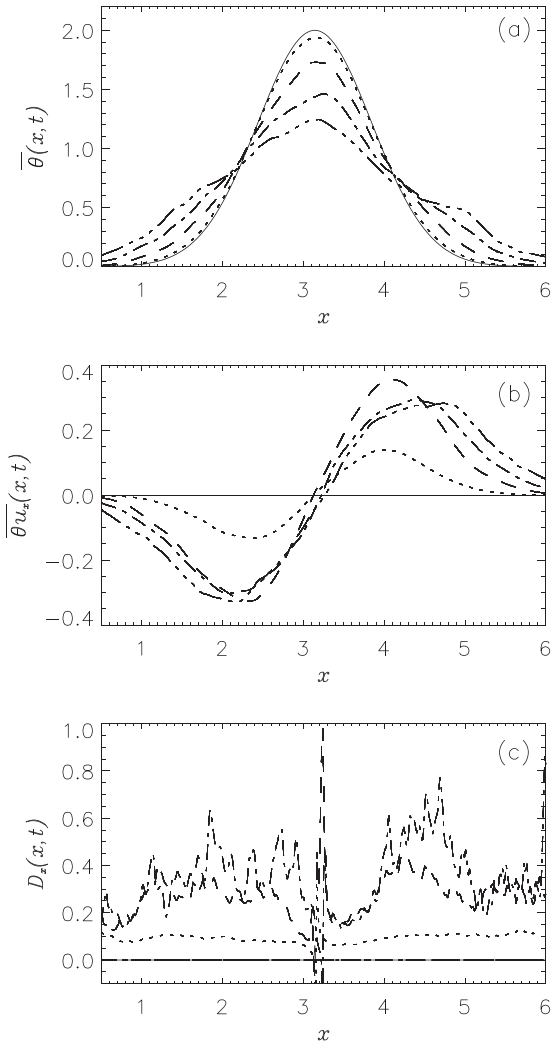

FIG. 10. (a) Averaged horizontal concentration $\overline{\theta}$ in run $A1_x$ (no rotation, no helicity) at times $t = 0$ (solid line), 0.5 (dotted line), 1 (dashed line), 1.25 (dashed-dotted line), and 1.5 (dashed-triple-dotted line). (b) Horizontal flux at the same times. (c) $\mathcal{D}_x(x,t)$ at the same times.

of helicity. Although in isotropic turbulence helicity does not affect significantly the energy scaling [14,22,55,56], an increase in the turbulent diffusion in the presence of helicity was predicted in [20]. Using renormalization group techniques, the authors estimated that turbulent diffusion in a helical flow can be up to a 50% larger than in a nonhelical flow. In our simulations, after averaging $\mathcal{D}_x$ over two simulations to decrease uncertainties, the averaged in time value of $\mathcal{D}_x(t)$ is $\approx 0.3 \pm 0.1$ for the nonhelical case and $\approx 0.44 \pm 0.07$ for the helical case, in reasonable agreement with the theoretical result. However, note that error bars are large. These errors could be decreased further by performing an ensemble of simulations to study $\mathcal{D}_x(t)$. Such a study is left for future work.

It is worth mentioning that the same analysis was performed in simulations $A1_z$ and $B1_z$ (i.e., the same runs but with an initial Gaussian profile in the z direction). As expected from the flow isotropy, the same behavior was obtained.

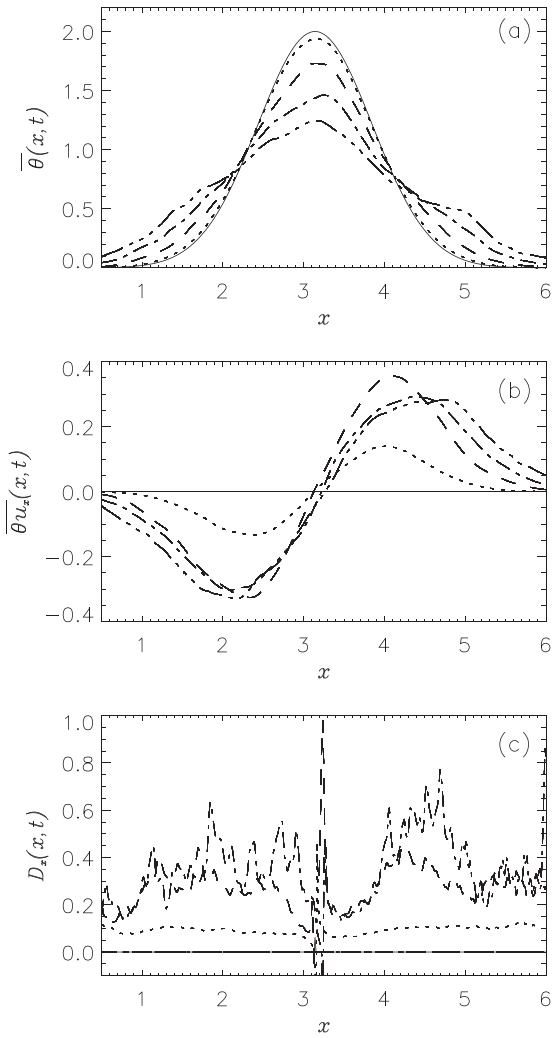

FIG. 11. (a) Averaged horizontal concentration $\overline{\theta}$ in run $B1_x$ (no rotation, helical) at times $t = 0$ (solid line), 0.5 (dotted line), 1 (dashed line), 1.25 (dashed-dotted line), and 1.5 (dashed-triple-dotted line). (b) Horizontal flux at the same times. (c) $\mathcal{D}_x(x,t)$ at the same times.

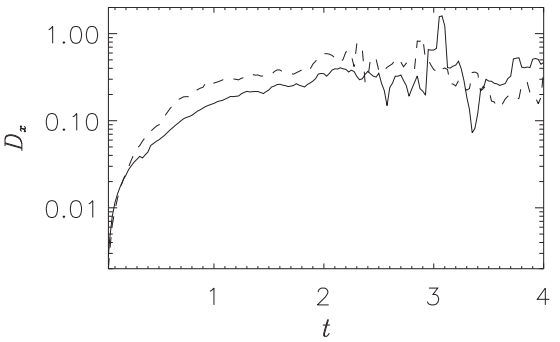

FIG. 12. Horizontal turbulent diffusion as a function of time for runs $A1_x$ (solid line, no rotation and no helicity) and $B1_x$ (dashed line, no rotation but with helical forcing). The diffusion coefficient averaged over the steady state, and for each case averaged over two simulations as the ones shown in this figure, is $\mathcal{D}_x = 0.3 \pm 0.1$ for the nonhelical case and $\mathcal{D}_x = 0.44 \pm 0.07$ for the helical case.

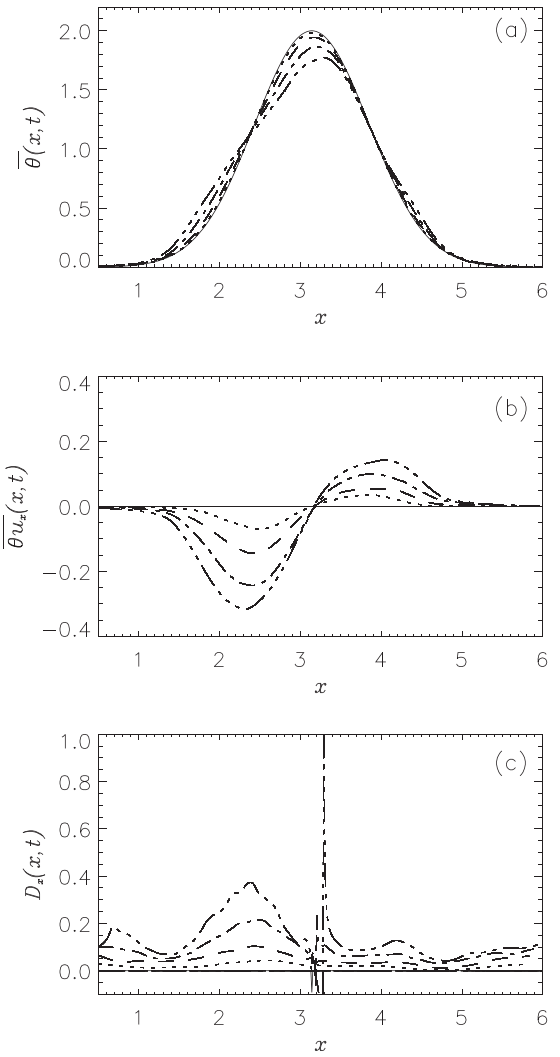

FIG. 13. (a) Averaged horizontal concentration $\overline{\theta}$ in run $B3_x$, at times $t = 0$ (solid line), 0.25 (dotted line), 0.5 (dashed line), 0.75 (dashed-dotted line), and 1 (dashed-triple-dotted line). (b) Horizontal flux at the same times. (c) $\mathcal{D}_x(x,t)$ at the same times.

C. Rotating helical turbulence

1. *Horizontal diffusion*

Figure 13 shows the mean profile of the passive scalar $\overline{\theta}(x,t)$, the horizontal flux $\overline{\theta u_x}(x,t)$, and the pointwise value of $\mathcal{D}_x(x,t)$ at five different times for run $B3_x$ (helical and with Ro = 0.01). In this case, note that the average profile and the flux become asymmetric, i.e., there is an excess of concentration of $\overline{\theta}(x,t)$ for $x < \pi$, and the absolute value of the flux is larger for $x < \pi$ than for $x > \pi$. This asymmetry is caused by the Coriolis force and has been previously observed for rotating nonhelical flows in [12,14]. In our runs, the passive scalar at $t = 0$ is concentrated in a narrow band around $x = \pi$. The average flux is thus towards positive values of x for $x > \pi$ and towards negative values of x for $x < \pi$ (i.e., in the direction of $-\nabla\theta$, see, for instance, Fig. 13). The Coriolis force in Eq. (1) is $-2\Omega\hat{z} \times \mathbf{u}$, and creates an overturning in the $x - y$ plane of the initially only dependent on x Gaussian profile, as will be shown later in more detail in spatial visualizations of the

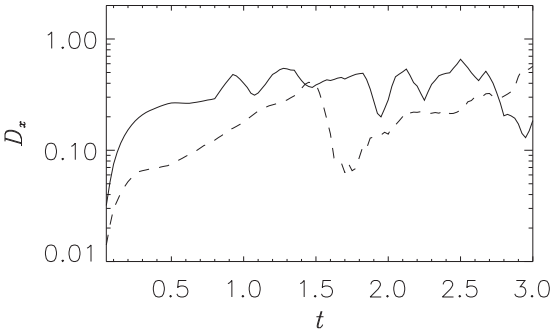

FIG. 14. Horizontal turbulent diffusion as a function of time for runs $A2_x$ (solid) and $B2_x$ (dashed) (Ro = 0.02, respectively, without and with helicity). The diffusion coefficient averaged over the steady state, and for each case averaged over two simulations as the ones shown in this figure, is $\mathcal{D}_x = 0.40 \pm 0.06$ for the nonhelical case and $\mathcal{D}_x = 0.2 \pm 0.1$ for the helical case.

passive scalar. This overturning also results in the asymmetry observed in Fig. 13 (for more details, see also [14]).

By computing the mean value of $\mathcal{D}_x(x,t)$ over the spatial coordinate, we obtain the turbulent diffusion coefficient. Figure 14 shows first the horizontal turbulent diffusion as a function of time for runs $A2_x$ and $B2_x$ (both with Ro = 0.02, without and with helicity, respectively), and then Fig. 15 shows the same quantity for runs $A3_x$ and $B3_x$ (Ro = 0.02, without and with helicity, respectively). For both rotation rates, we observe that horizontal diffusion is smaller in the presence of helicity. This result is the opposite to that observed for the isotropic runs in the previous section, for which helicity slightly increased the turbulent diffusion.

As already mentioned, while in isotropic turbulence helicity does not affect the energy spectrum scaling [14,22,55,56], in rotating turbulence the presence of helicity results in shallower horizontal spectrum for the energy, in comparison with rotating nonhelical turbulence [14,22]. As a result, a smaller turbulent diffusion can be expected, as small-scale velocity field fluctuations should be less energetic in the helical rotating case. Indeed, in most two point closure models, the turbulent diffusivity is proportional to the mean kinetic energy

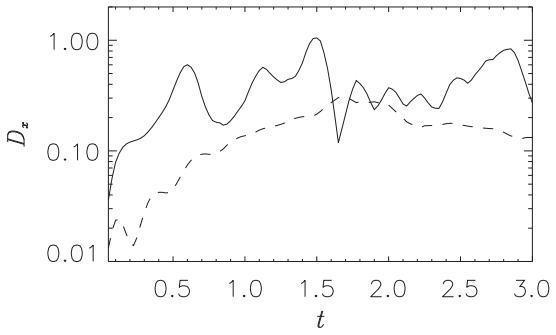

FIG. 15. Horizontal turbulent diffusion as a function of time for runs $A3_x$ (solid line) and $B3_x$ (dashed line) (Ro = 0.01, respectively, without and with helicity). The diffusion coefficient averaged over the steady state, and for each case averaged over two simulations as the ones shown in this figure, is $\mathcal{D}_x = 0.4 \pm 0.1$ for the nonhelical case and $\mathcal{D}_x = 0.19 \pm 0.06$ for the helical case.

in the turbulent fluctuations, $\overline{u^2}/2$, and if the kinetic energy spectrum is steeper, then the diffusivity should decrease. A simple mean field argument can illustrate this. We can split the velocity in a mean flow $\overline{\mathbf{u}}$, and a fluctuating component $\mathbf{u}'$, such that $\mathbf{u} = \overline{\mathbf{u}} + \mathbf{u}'$. In our runs, $\overline{\mathbf{u}} = 0$ and $\mathbf{u} = \mathbf{u}'$. Splitting the passive scalar in the same way we have $\theta = \overline{\theta} + \theta'$. Replacing in Eq. (2) and averaging we obtain

$$\frac{\partial \overline{\theta}}{\partial t} = -\boldsymbol{\nabla} \cdot (\overline{\mathbf{u}\theta'}), \tag{33}$$

and subtracting this equation from Eq. (2) we then obtain

$$\frac{\partial \theta}{\partial t} = -\boldsymbol{\nabla} \cdot (\mathbf{u}\overline{\theta}). \tag{34}$$

We can integrate this last equation assuming the flow is correlated over the integral eddy turnover time τ, to obtain

$$\theta' \approx -\tau \boldsymbol{\nabla} \cdot (\mathbf{u}\overline{\theta}) = -\tau \mathbf{u} \cdot \boldsymbol{\nabla}\overline{\theta}, \tag{35}$$

where incompressibility was used. Then, replacing in Eq. (33),

$$\frac{\partial \overline{\theta}}{\partial t} \approx \frac{\partial}{\partial x_i}\left(\tau \overline{u_i u_j} \frac{\partial \overline{\theta}}{\partial x_j}\right), \tag{36}$$

where the coefficient $\tau\overline{u_i u_j}$ can be interpreted as a turbulent diffusion. If the flow is isotropic, then $\mathcal{D} \approx \tau\overline{u^2}$. A more refined mean field derivation of this expression can be found in [21,57,58], while two point closure derivations can be found in [59,60].

Although the argument above is only illustrative, it gives an interesting hint to the possible cause of the reduced perpendicular diffusion in helical rotating flows. As the perpendicular energy spectrum in this case is steeper than in the absence of helicity, then the smaller energy at small scales results in less mixing and diffusion.

2. *Vertical diffusion*

Figure 16 shows the mean vertical passive scalar concentration $\overline{\theta}(z)$, the mean vertical flux $\overline{\theta v_z}(z)$, and the pointwise value of $\mathcal{D}_z(z)$ at different times in run $B3_z$. In this case, the profiles are more similar to those obtained in the isotropic and homogeneous case: $\overline{\theta}(z)$ and $\overline{\theta v_z}(z)$ are, respectively, symmetric and antisymmetric with respect to $z = \pi$.

As in the case of horizontal diffusion, we can obtain the vertical turbulent diffusion coefficient as a function of time by computing the mean value of $\mathcal{D}_z(z,t)$ for all values of z. Figure 17 shows $\mathcal{D}_z(t)$ for runs $A3_z$ and $B3_z$ (both with Ro = 0.01, respectively, without and with helicity). Note that horizontal turbulent diffusion is larger in the presence of helicity.

D. Spatial distribution and structures

Results shown above suggest that both horizontal and vertical diffusion are affected by rotation and by the presence of helicity. Figure 18 shows a horizontal slice of the passive scalar concentration in runs $A3_x$ and $B3_x$ at $t = 1$ (i.e., around the time the turbulent diffusion coefficients $\mathcal{D}_x$ and $\mathcal{D}_z$ reach a turbulent steady value). As also observed in [14], the initial Gaussian profile in the nonhelical rotating flow (run $A5_x$) diffuses in time, and also bends and rotates. As previously

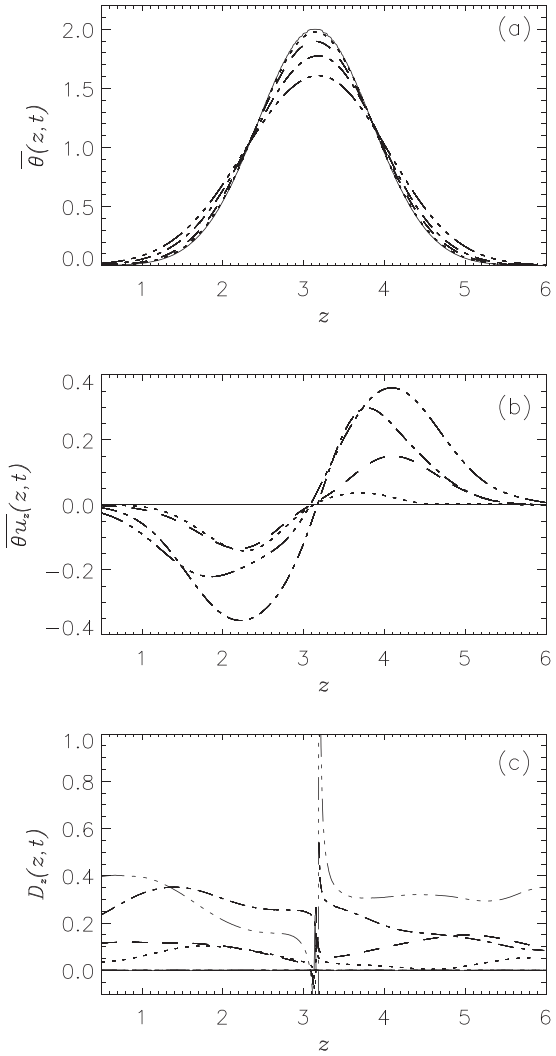

FIG. 16. Averaged vertical concentration $\overline{\theta}$ in run $B3_z$, at times $t = 0$ (solid line), 0.25 (dotted line), 0.5 (dashed line), 0.75 (dashed-dotted line), and 1 (dashed-triple-dotted line). (b) Horizontal flux at the same times. (c) $\mathcal{D}_x(x,t)$ at the same times.

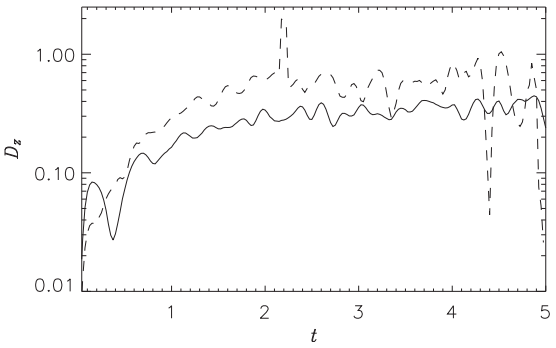

FIG. 17. Vertical turbulent diffusion as a function of time for runs $A3_z$ (solid line) and $B3_z$ (dashed line). The former run has no net helicity, while the latter has helical forcing. The diffusion coefficient averaged over the steady state is $\mathcal{D}_x = 0.34 \pm 0.04$ for the nonhelical case and $\mathcal{D}_x = 0.6 \pm 0.1$ for the helical case.

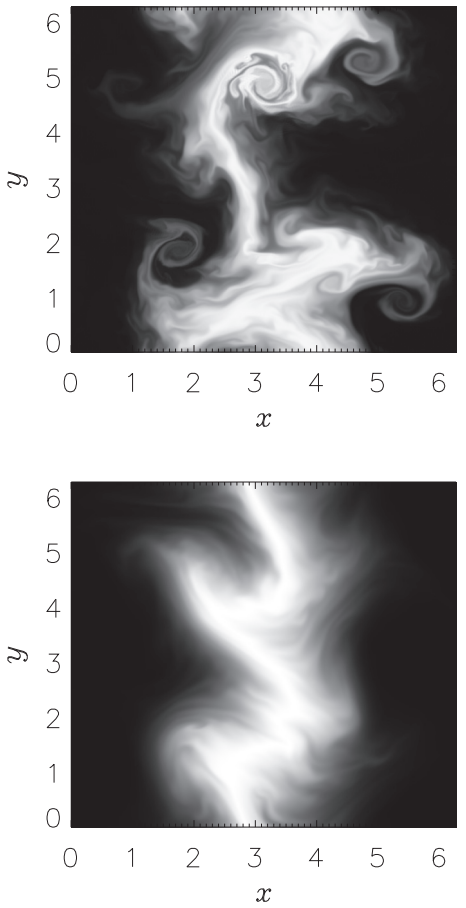

FIG. 18. Passive scalar concentration in a horizontal slice of runs $A3_x$ (left) and $B3_x$ (right) at time $t = 1$. Note how the initial concentration (Gaussian, centered around $x = \pi$, and independent of the y coordinate) gets distorted and diffused.

mentioned, the overturning of the profile is caused by the Coriolis force (see also [12]). In the helical rotating flow (run $B3_x$), we also observe this overturning, although the initial profile is less diffused (as indicated, e.g., by the most extreme values in the x coordinate for which a significant concentration of the passive scalar can be observed, which are larger in run $A5_x$).

Diffusion in the parallel direction in rotating flows is of a different nature than vertical diffusion (see Fig. 19, which shows vertical slices of the passive scalar concentration in runs $A3_z$ and $B3_z$ at $t = 0.5$ and 1.5). In the rotating nonhelical case, the passive scalar initial profile is diffused in vertical stripes, created by updrafts or downdrafts inside columnar structures of the velocity field [14]. These columnar structures in the velocity and vorticity fields have been reported in rapidly rotating flows, and are associated with the bidimensionalization of the flow [28,40,61]. Recently, these columns were also observed to efficiently transport particles along the direction of the axis of rotation, in a so-called "elevator effect" [62]. As time increases, the stripes observed in the passive scalar in Fig. 19 are further stretched, resulting in larger mixing and diffusion. Note, however, that in the presence of helicity, the stripes are increased even further, in good agrement with the increased diffusion in helical flows reported

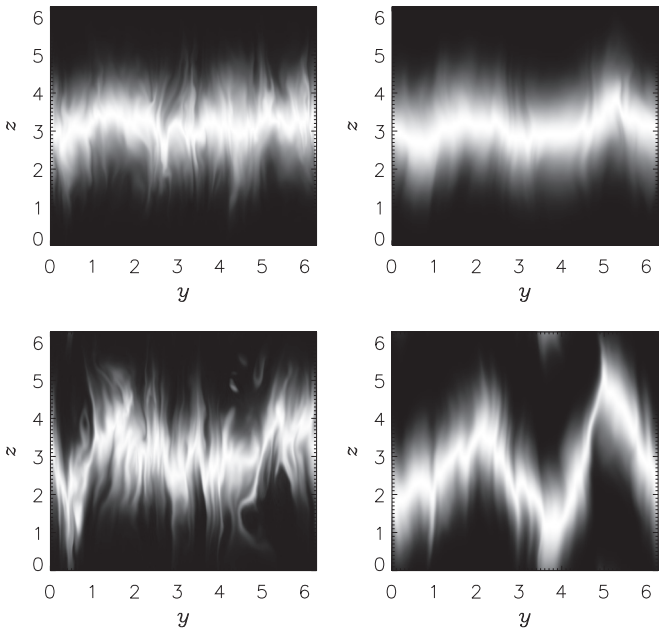

FIG. 19. Passive scalar concentration in a vertical slice of runs $A3_z$ (left) and $B3_z$ (right) at time $t = 0.5$ (top row) and at time $t = 1.5$ (bottom row).

above. This can be understood as the presence of helicity in the flow requires the three components of the velocity to be nonzero, resulting in a more three-dimensional flow. In all cases, from the visualization of the passive scalar in real space, it can be observed that the passive scalar displays strong gradients concentrated along surfacelike regions (which in the rotating case tend to be aligned with the rotation axis), in good agreement with the codimension of $C_0 \approx 0.65$ found in the multifractal model in Sec. III D.

V. CONCLUSIONS

We analyzed data from direct numerical simulations of advection and diffusion of a passive scalar in rotating helical and nonhelical turbulent flows. A total of 18 simulations with spatial resolution of 512^3 grid points were performed, using different Reynolds and Rossby numbers, and changing the forcing and initial conditions of the passive scalar, to measure energy and passive scalar spectra, anisotropic velocity and passive scalar structure functions, probability density functions, and diffusion coefficients in the directions parallel and perpendicular to the rotation's axis.

In the first part of the paper, we studied scaling laws of the energy and passive scalar variance, using spectra and structure functions in the horizontal and vertical directions. We showed that helicity affects the inertial range scaling of the passive scalar, with its variance following a spectral law consistent with $\sim k_\perp^{-1.4}$. This scaling is shallower than the one found for passive scalars in nonhelical rotating turbulence [14], and consistent with a phenomenological argument that states that if the energy follows a power law $\sim k^{-n}$ in the inertial range, then the passive scalar variance should follow a power law $\sim k^{-n_\theta}$ with $n_\theta = (5-n)/2$. This argument, already proposed in [14] for rotating and nonrotating nonhelical flows and which follows from Kolmogorov-Obhukov scaling, was found here to uphold also in the presence of helicity. The study of structure functions confirms these scaling laws, and indicates that the passive scalar is more anisotropic at small scales than velocity field. Also, the passive scalar was found to be more intermittent than the velocity field, a well known result, and which becomes more pronounced in the presence of rotation and of helicity. The anomalous scaling exponents for the passive scalar can be approximated using Kraichnan's model with the second-order exponent ζ_2 obtained from our phenomenological model, and with a dimensionality $d = 2$. As in the case of rotating nonhelical flows studied previously in [13], this value of d was interpreted as a result of the quasibidimensionalization of the distribution of the passive scalar in the presence of rotation. However, the fact that the velocity field itself is intermittent in our simulations, or at least that the velocity field has structures and is not completely random (unlike the velocity in Kraichnan's model), may also contribute to the increase in the intermittency of the passive scalar when compared with the $d = 3$ case. To obtain a better fit to the data, we also derived a multifractal model based on the She-Leveque model and on recent extensions of this model to consider the case of the passive scalar. The scaling exponents from the model are in better agreement with the data for a codimension of structures $C_0 \approx 0.65$, which is compatible with values previously obtained for the passive scalar in isotropic and homogeneous turbulence, and which indicates that the geometry of regions with strong scalar gradients is similar to that found in the absence of rotation (independently of the anisotropy).

In the second part of the paper, the analysis of the effective diffusion coefficients calculated from Fick's law suggests that for isotropic flows (i.e., without rotation) helicity increases turbulent diffusion, in agreement with previous models and theoretical predictions [19,20]. In the presence of rotation, results indicate that the overall effect of rotation (irrespectively of the content of helicity of the flow) is to decrease horizontal diffusion, while the effect on vertical diffusion is less pronounced. Helicity further decreases horizontal diffusion but increases vertical diffusion (compared with the nonhelical rotating case). The decrease in horizontal diffusion was explained with a simple model for turbulence diffusivity based on the available energy for the small-scale turbulent fluctuations.

ACKNOWLEDGMENTS

The authors acknowledge financial support from Grants No. PIP11220090100825, No. UBACYT 20020130100738, No. PICT 2011-1529, and No. PICT 2011-1626. P.D.M. acknowledges support from the Carrera del Investigador Científico of CONICET.

[1] K. R. Sreenivasan, Proc. R. Soc. London, Ser. A **434**, 165 (1991).
[2] Z. Warhaft, Annu. Rev. Fluid Mech. **32**, 203 (2000).
[3] R. H. Kraichnan, Phys. Rev. Lett. **72**, 1016 (1994).

[4] G. Falkovich, K. Gawedzki, and M. Vergassola, Rev. Mod. Phys. **73**, 913 (2001).
[5] E. Schatzman, Astron. Astrophys. **56**, 211 (1997).
[6] C. Charbonnel, S. Vauclair, and J.-P. Zahn, Astron. Astrophys. **255**, 191 (1992).
[7] G. Rudiger and V. Pipin, Astron. Astrophys. **375**, 149 (2001).
[8] P. H. Roberts and G. A. Glatzmaier, Rev. Mod. Phys. **72**, 1081 (2000).
[9] R. Rotunno and G. H. Bryan, J. Atmos. Sci. **69**, 2284 (2001).
[10] T. R. Osborn, J. Phys. Oceanogr. **10**, 83 (1980).
[11] G. T. Csanady, *Turbulent Diffusion in the Environment* (Kluwer Academic, Dordrecht, 1973).
[12] A. Brandenburg, A. Svedin, and G. M. Vasil, Mon. Not. R. Astron. Soc **395**, 1599 (2009).
[13] P. Rodriguez Imazio and P. D. Mininni, Phys. Rev. E **83**, 066309 (2011).
[14] P. Rodriguez Imazio and P. D. Mininni, Phys. Rev. E **87**, 023018 (2013).
[15] A. Celani, M. Cencini, A. Mazzino, and M. Vergassola, New J. Phys. **6**, 72 (2004).
[16] R. Komm, F. Hill, and R. Howe, J. Phys.: Conf. Ser. **118**, 012035 (2008).
[17] G. Rudiger, L. L. Kitchatinov, and A. Brandenburg, Solar Phys. **269**, 3 (2010).
[18] H. K. Moffat, J. Fluid Mech. **41**, 435 (1970).
[19] H. K. Moffat, Reg. Prog. Phys. **46**, 621 (1983).
[20] O. G. Chkhetiani, M. Hnatich, E. Jurčišinová, M. Jurčišin, A. Mazzino, and M. Repašan, Phys. Rev. E **74**, 036310 (2006).
[21] T. Elperin, N. Kleeorin, I. Rogachevskii, and D. Sokoloff, Phys. Rev. E **61**, 2617 (2000).
[22] P. D. Mininni and A. Pouquet, Phys. Rev. E **79**, 026304 (2009).
[23] A. Vincent, G. Michaud, and M. Meneguzzi, Phys. Fluids **8**, 1312 (1996).
[24] P. K. Yeung and J. Xu, Phys. Fluids **16**, 93 (2004).
[25] P. K. Yeung and Y. Zhou, Phys. Fluids **10**, 2895 (1998).
[26] L. M. Smith and F. Waleffe, Phys. Fluids **11**, 1608 (1999).
[27] C. Cambon, F. S. Godeferd, F. C. G. A. Nicolleau, and J. C. Vassilicos, J. Fluid Mech. **499**, 231 (2004).
[28] P. A. Davidson, P. J. Staplehurst, and S. B. Dalziel, J. Fluid Mech. **557**, 135 (2006).
[29] W. C. Müller and M. Thiele, Europhys. Lett. **77**, 34003 (2007).
[30] P. D. Mininni and A. Pouquet, Phys. Fluids **22**, 035105 (2010).
[31] D. O. Gómez, P. D. Mininni, and P. Dmitruk, Adv. Sp. Res. **35**, 899 (2005).
[32] P. D. Mininni, D. Rosenberg, R. Reddy, and A. Pouquet, Parallel Computing **37**, 316 (2011).
[33] A. Pouquet and G. S. Patterson, J. Fluid Mech. **85**, 305 (1978).
[34] I. Arad, B. Dhruva, S. Kurien, V. S. L'vov, I. Procaccia, and K. R. Sreenivasan, Phys. Rev. Lett. **81**, 5330 (1998).
[35] L. Biferale and M. Vergassola, Phys. Fluids **13**, 2139 (2001).
[36] L. Biferale and I. Procaccia, Phys. Rep. **414**, 43 (2005).
[37] P. D. Mininni and A. Pouquet, Phys. Fluids **22**, 035106 (2010).
[38] R. Benzi, S. Ciliberto, R. Tripiccione, C. Baudet, F. Massaioli, and S. Succi, Phys. Rev. E **48**, R29 (1993).
[39] R. Benzi, S. Ciliberto, C. Baudet, G. R. Chavarria, and R. Tripiccione, Europhys. Lett. **24**, 275 (1993).
[40] C. Cambon and L. Jacquin, J. Fluid Mech. **202**, 295 (1989).
[41] F. Waleffe, Phys. Fluids A **5**, 677 (1993).
[42] C. Cambon, N. N. Mansour, and F. S. Godeferd, J. Fluid Mech. **337**, 303 (1997).
[43] A. Pouquet and P. D. Mininni, Philos. Trans. R. Soc., A **368**, 1635 (2010).
[44] C. Baraud, B. B. Plapp, H. L. Swinney, and Z. S. She, Phys. Fluids **15**, 2091 (2003).
[45] J. Seiwert, C. Morize, and F. M. Phys, Phys. Fluids **20**, 071702 (2008).
[46] P. D. Mininni, A. Alexakis, and A. Pouquet, Phys. Rev. E **77**, 036306 (2008).
[47] P. D. Mininni, A. Alexakis, and A. Pouquet, Phys. Fluids **21**, 015108 (2009).
[48] E. Deusebio, G. Boffetta, E. Lindborg, and S. Musacchio, Phys. Rev. E **90**, 023005 (2014).
[49] Z. S. She and E. Leveque, Phys. Rev. Lett. **72**, 336 (1994).
[50] N. Cao and S. Chen, Phys. Fluids **9**, 1203 (1997).
[51] C. M. de Silva, J. Philip, K. Chauhan, C. Meneveau, and I. Marusic, Phys. Rev. Lett. **111**, 044501 (2013).
[52] A. S. Monin and M. Yaglom, *Statistical Fluid Mechanics: Mechanics of Turbulence* (MIT Press, Cambridge, 1975).
[53] K. R. Sreenivasan, Annu. Rev. Fluid Lett. **23**, 539 (1991).
[54] H. Politano and A. Pouquet, Phys. Rev. E **52**, 636 (1995).
[55] Q. Chen, S. Chen, and G. L. Eyink, Phys. Fluids **15**, 361 (2003).
[56] Q. Chen, S. Chen, G. L. Eyink, and D. D. Holm, Phys. Rev. Lett. **90**, 214503 (2003).
[57] E. Blakman and G. Field, Phys. Fluids **15**, L73 (2003).
[58] A. Brandenburg, K. H. Rädler, and H. Kemel, Astron. Astrophys. **539**, A35 (2012).
[59] R. H. Kraichnan, J. Fluid Mech. **77**, 753 (1976).
[60] J. R. Herring, M. Schertzer, and M. Lesieur, J. Fluid Mech. **124**, 411 (1982).
[61] F. Waleffe, Phys. Fluids A **4**, 350 (1992).
[62] L. Biferale, F. Bonaccorso, I. M. Mazzitelli, M. A. T. van Hinsberg, A. S. Lanotte, S. Musacchio, P. Perlekar, and F. Toschi, Phys. Rev. X **6**, 041036 (2016).